Photodissociation dynamics of the CNN free radical

Ryan T. Bise, Alexandra A. Hoops, Hyeon Choi,[a] and Daniel M. Neumark[b]
Department of Chemistry, University of California, Berkeley, California 94720 and Chemical Sciences Division, Lawrence Berkeley National Laboratories, Berkeley, California 94720

(Received 11 May 2000; accepted 14 June 2000)

The spectroscopy and photodissociation dynamics of the $\tilde{A}\,^3\Pi$ and $\tilde{B}\,^3\Sigma^-$ states of the CNN radical have been investigated by fast beam photofragment translational spectroscopy. Vibronic transitions located more than 1000 cm^{-1} above the $\tilde{A}\,^3\Pi \leftarrow \tilde{X}\,^3\Sigma^-$ origin were found to predissociate. Photofragment yield spectra for the $\tilde{B}\,^3\Sigma^- \leftarrow \tilde{X}\,^3\Sigma^-$ band between 40 800 and 45 460 cm^{-1} display resolved vibrational progressions with peak spacing of $\approx$1000 cm^{-1} corresponding to symmetric stretch 1_0^n and combination band $1_0^n 3_0^1$ progressions. Ground state products $C(^3P)+N_2$ were found to be the major photodissociation channel for both the $\tilde{A}\,^3\Pi$ and $\tilde{B}\,^3\Sigma^-$ states. The translational energy distributions for the $\tilde{A}\,^3\Pi$ state are bimodal with high and low translational energy components. The distributions for the $\tilde{B}\,^3\Sigma^-$ state reveal partially resolved vibrational structure for the N_2 photofragment and indicate extensive vibrational and rotational excitation of this fragment. These results suggest that bent geometries are involved in the dissociation mechanism and provide more accurate values: $\Delta_f H_0(CNN)=6.16\pm0.05$ eV and $\Delta_f H_{298}(CNN)=6.15\pm0.05$ eV. These values, coupled with recent $D_0(RH)$ and $D_{298}(RH)$ values from Clifford *et al.* [J. Phys. Chem. **102**, 7100 (1998)], yield $\Delta_f H_0(HCNN)=5.02\pm0.18$ eV, $\Delta_f H_{298}(HCNN)=4.98\pm0.18$ eV, $\Delta_f H_0(H_2CNN)=3.09\pm0.21$ eV, and $\Delta_f H_0(H_2CNN)=3.09\pm0.21$ eV. © *2000 American Institute of Physics.* [S0021-9606(00)01334-9]

I. INTRODUCTION

The CNN free radical is a potentially important combustion intermediate. It has been proposed as an intermediate in the mechanism for the formation of transient NO in the primary reaction zone of premixed flames of hydrocarbons with N_2–O_2 mixtures,[1] because it can provide a low energy pathway for the cleavage of N_2 to produce N atoms through the reaction $C+N_2 \rightarrow N+CN$. The resulting N atoms are rapidly oxidized to nitric oxide. To assess the importance of the CNN radical in combustion processes, accurate values for the dissociation energy, heat of formation, and a better understanding of the $C+N_2$ potential energy surface is required. In order to address these issues, we have investigated the photodissociation spectroscopy and dynamics of CNN.

The CNN radical, like other 14 valence electron systems, has attracted interest from both experimentalists and theorists regarding its bonding and geometry. Most spectroscopic studies of this radical have been performed in rare gas matrices. Electron spin resonance experiments[2,3] determined that the ground state symmetry is $^3\Sigma^-$. The first infrared absorption measurements on CNN revealed transitions at 1241, 393, and 2847 cm^{-1} that were assigned to fundamentals ν_1(symmetric stretch), ν_2(bend), and ν_3(asymmetric stretch), respectively.[4,5] More recent Fourier transform/laser-induced fluorescence (FT-LIF) emission studies in an Ar matrix[6] found the ground state asymmetric stretch (ν_3) to be 1419 cm^{-1}, suggesting that the intensity of the infrared fundamental transition is ''accidentally'' zero and that the transition observed at 2847 cm^{-1} in previous work is the ν_3 overtone. With this new value for the ν_3 frequency, similar force constants were found for the C–N and N–N bonds, indicating that both are double bonds.

Several excited electronic states of CNN have also been observed in matrix ultraviolet absorption and emission studies. UV absorption bands near 23 870 and 25 250 cm^{-1} in a number of different rare gas matrices have been reported and have been subsequently assigned to the CNN radical.[4,7–10] Bondybey and English[11] have observed analogous bands in their laser-induced fluorescence (LIF) studies in an Ar matrix, assigning the transitions to the $\tilde{A}\,^3\Pi \leftarrow \tilde{X}\,^3\Sigma^-$ band. These authors reported values for the spin–orbit splitting, Renner–Teller parameter, and vibrational frequencies for the $\tilde{A}\,^3\Pi$ state. Higher energy absorption bands were observed by Jacox.[12] One band between 40 000–47 000 cm^{-1}, assigned to the $\tilde{B}\,^3\Sigma^- \leftarrow \tilde{X}\,^3\Sigma^-$ transition, displayed two main progressions with peak spacing of $\approx$1000 cm^{-1} while absorptions at 49 116 and 48 543 cm^{-1} in N_2 and Ar matrices, respectively, were associated with a different electronic transition.

Gas-phase optical spectroscopic data for CNN is limited to low resolution UV absorption studies by Braun *et al.*,[13] who observed transitions at 23 870 and 25 190 cm^{-1}, and a rotationally resolved LIF spectrum of the $\tilde{A}\,^3\Pi \leftarrow \tilde{X}\,^3\Sigma^-$ origin by Curtis *et al.*,[14] yielding a gas-phase spin–orbit splitting, $A=-26.5\ cm^{-1}$. These authors also reported a sequence band $\approx$ 145 cm^{-1} above the origin.

[a]Current address: Department of Chemistry and Biochemistry, University of California, Los Angeles, California 90095-1569.
[b]Author to whom correspondence should be addressed. Electronic mail: dan@radon.cchem.berkeley.edu

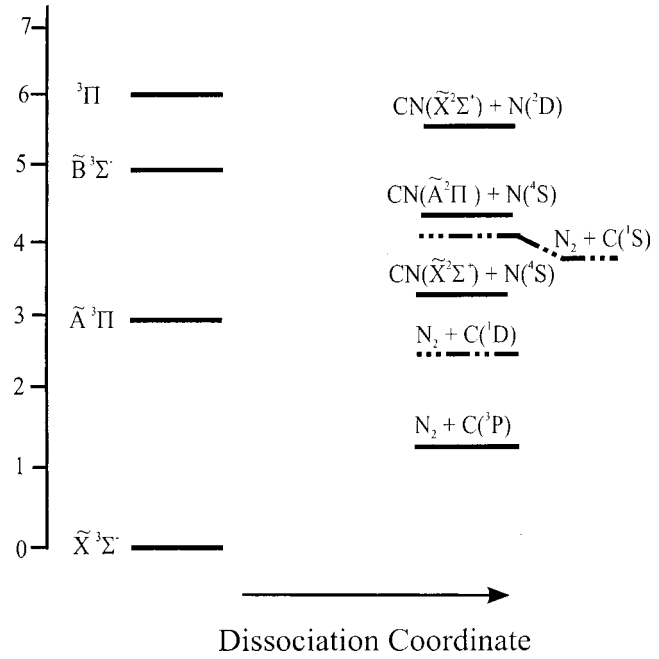

FIG. 1. Energy level diagram of the excited triplet states of CNN and dissociation product states. The relative energetic position of the $\tilde{A}\,^3\Pi$ state is based on the work of Curtis *et al.* (Ref. 14) and the $\tilde{B}\,^3\Sigma^-$ and $\tilde{C}\,^3\Pi$ states are from the studies by Jacox (Ref. 12). The dissociation energies have been determined from this work.

Recently, the gas-phase photoelectron spectrum of the CNN^- anion was measured by Clifford *et al.*[15] providing the electron affinity of CNN, 1.771 ± 0.010 eV, as well as the ground state neutral frequencies. The photoelectron spectrum is dominated by the vibrational origin band, indicating very similar geometries for the anion and neutral. From their electron affinities of CNN and HCNN along with other thermochemical data, the authors determined $\Delta_f H_0(\mathrm{CNN}) = 5.9 \pm 0.2$ eV, which is well within the error bars for the previously reported value of 6.6 ± 1.0 eV by Gurvich.[16]

The electronic structure of CNN has been investigated in numerous theoretical studies. According to Walsh's rules,[17] all of the relevant electronic states for this 14 valence electron system, shown in Fig. 1, are predicted to be linear with the dominant molecular orbital configurations shown below:

$$\ldots(6\sigma)^2(1\pi)^4(7\sigma)^2(2\pi)^2 \quad \tilde{X}\,^3\Sigma^-, \tilde{a}\,^1\Delta, \tilde{b}\,^1\Sigma^+,$$

$$\ldots(6\sigma)^2(1\pi)^4(7\sigma)^1(2\pi)^3 \quad \tilde{A}\,^3\Pi, {}^1\Pi,$$

$$\ldots(6\sigma)^2(1\pi)^3(7\sigma)^2(2\pi)^3 \quad \tilde{B}\,^3\Sigma^-,$$

$$\ldots(6\sigma)^1(1\pi)^4(7\sigma)^2(2\pi)^3 \quad {}^3\Pi.$$

DeKock *et al.*[5] examined the infrared frequencies, finding the geometry and force constants to be highly dependent on the theoretical method employed and were not able to produce the experimental values observed by Milligan and Jacox. More recent *ab initio* calculations by Suter *et al.*[18] yielded ground state vibrational frequencies in good agreement with the newer experimental values.[6] Configuration interaction methods were applied to the $\tilde{X}\,^3\Sigma^-$, $\tilde{a}\,^1\Delta$, $\tilde{A}\,^3\Pi$, and $^1\Pi$ states,[19] yielding a calculated fluorescence lifetime value for the $\tilde{A}\,^3\Pi$ state of 216 ns in good agreement with the reported experimental lifetimes of 220 and 280 ns from matrix LIF emission studies.[11,19] Clifford *et al.*[15] have used *ab initio* methods to calculate the electron affinity, excited state term energies, and ground state vibrational frequencies for the CNN radical. Their results compare favorably with their experimental photoelectron spectroscopy measurements. Martin *et al.*[20] have performed *ab initio* calculations on the linear, bent, and cyclic states of NCN and CNN examining possible intermediates and pathways towards isomerization.

Our interest in the CNN radical has been further motivated by our recent study of the dissociation dynamics of the structural isomer NCN,[21] which dissociates to $N_2 + C(^3P)$ products via a cyclic transition state. The work presented here on the photodissociation dynamics of the CNN radical further characterizes the global potential energy surface for CN_2 species. Using the technique of fast beam photofragment translational spectroscopy, we have examined the photodissociation spectroscopy and dynamics of the $\tilde{A}\,^3\Pi \leftarrow \tilde{X}\,^3\Sigma^-$ and $\tilde{B}\,^3\Sigma^- \leftarrow \tilde{X}\,^3\Sigma^-$ bands of CNN. Vibrational levels of the $\tilde{A}\,^3\Pi$ state lying >1000 cm^{-1} above the origin predissociate to photoproducts $C(^3P) + N_2$. Extended progressions of the $\tilde{B}\,^3\Sigma^- \leftarrow \tilde{X}\,^3\Sigma^-$ band are observed between 40 820–45 450 cm^{-1}. Translational energy ($P(E_T)$) distributions show $C + N_2$ as the dominant dissociation channel with extensive rotational excitation the N_2 photofragment, indicating that intermediate bent states are involved along the dissociation pathway.

II. EXPERIMENT

The fast beam photofragment translational spectrometer[22–24] used in these studies is shown in Fig. 2. In this instrument, we generate a clean source of neutral radicals by mass-selectively photodetaching a beam of stable negative ions. The neutral radicals are photodissociated by a second laser and the photofragments detected with high efficiency.

CNN^- ions are generated in our pulsed discharge source described previously.[25] A mixture of 5:1 Ar:N_2O with a stagnation pressure of 2 atm is passed through a bubbler containing diazomethane (−78 °C). The resulting mixture is super-

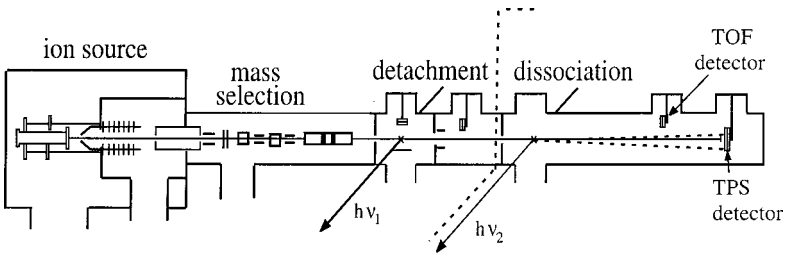

FIG. 2. Fast beam photofragment translational spectrometer. The dotted line separates the radical production section on the left from the photodissociation experiment on the right.

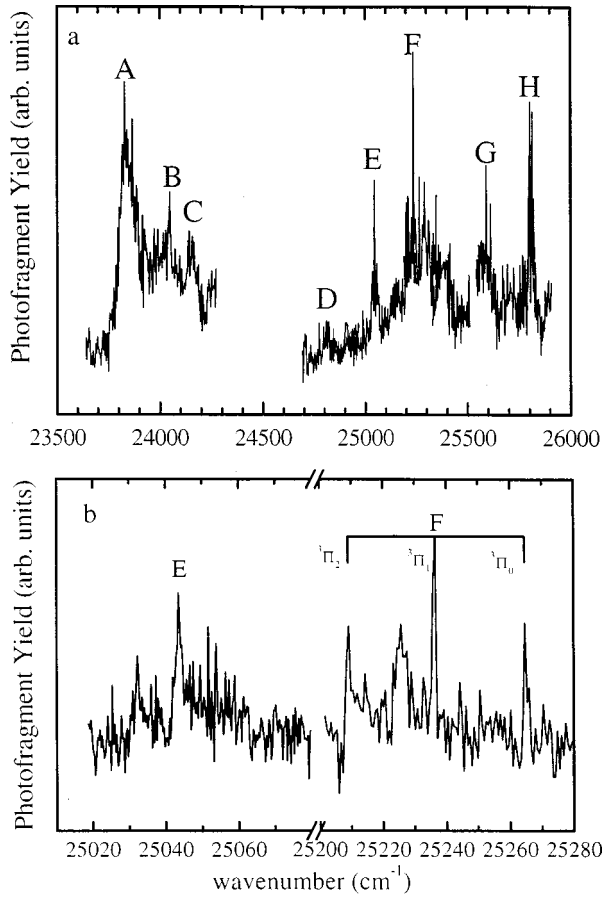

FIG. 3. (a) Photofragment yield spectrum of the $\tilde{A}\,^3\Pi \leftarrow \tilde{X}\,^3\Sigma^-$ band of CNN. (b) Expanded views of features E and F. The spin–orbit splitting for band F is illustrated with the comb denoting the Q-type transitions of the $^3\Pi_{2,1,0}$ states.

sonically expanded through a pulsed valve into a pulsed electric discharge, generating vibrationally and rotationally cold negative ions. Diazomethane was prepared from N-nitroso-N-methyl urea and 50% wt KOH.[26] Analysis of the photofragment yield spectra indicates that the rotational temperature of the anions is ≈50 K. The negative ions generated in the source region are accelerated to 8 keV, separated temporally by a Bakker time-of-flight (TOF) mass spectrometer,[27,28] and selectively photodetached by an excimer-pumped dye laser operating at 2.48 eV. This photodetachment energy, based on the photoelectron spectrum of Clifford *et al.*,[15] predominantly populates the $v=0$ level (≈ 90%) of the CNN $\tilde{X}\,^3\Sigma_g^-$ state. Any remaining ions are deflected out of the beam path.

In the dissociation region a second excimer-pumped dye laser intersects the CNN radical. A fraction of the neutrals absorb and dissociate yielding photofragments detected directly by either the TOF or TPS (time and position sensing) microchannel plate detector assemblies shown in Fig. 2. An aluminum strip is positioned at the center of each detector to prohibit undissociated radicals from impacting the detector, so that the observed signal is entirely from recoiling photofragments.

Two types of experiments are performed. First, the spectroscopy of the dissociative electronic states is examined by scanning the dissociation laser and monitoring the total flux of photofragments arriving at the retractable TOF detector, located at 0.68 m from the dissociation laser. The resulting photofragment yield (PFY) spectra is complementary to absorption and fluorescence measurements. We examined the photolysis of CNN between 23 700–26 000 cm^{-1} and 40 800–48 300 cm^{-1}. The fundamental output of the dye laser with a bandwidth of 0.3 cm^{-1} was used between 23 700–26 000 cm^{-1}. The dye laser was frequency-doubled to produce photon energies between 40 800–48 300 cm^{-1} with a bandwidth of 0.5 cm^{-1}.

Once the spectroscopy of the dissociative states has been examined, the dissociation dynamics at selected photolysis energies are investigated. In this experiment, both photofragments from a single parent radical are detected in coincidence using a time and position sensing (TPS) detector based on the concept developed by de Bruijn and Los.[29] Our implementation of this detection scheme has been described previously.[22,23] The TPS detector records the positions and difference in arrival time of the two photofragments from a single dissociation event. This information is then used to determine the masses of the fragments, their relative translational energy E_T, and the scattering angle θ between the relative velocity vector and the electric vector of the polarized dissociation laser. The photofragment mass resolution is $m/\Delta m \approx 10$ while the translational energy resolution for these experiments is $\Delta E_T/E_T = 2.0\%$. As discussed previously,[21] the relatively poor mass resolution for the photofragments is due to the size of the radical beam at the TPS detector.

III. RESULTS

A. Photofragment yield spectra, $\tilde{A}\,^3\Pi \leftarrow \tilde{X}\,^3\Sigma^-$ transitions

The photofragment cross section for the $\tilde{A}\,^3\Pi \leftarrow \tilde{X}\,^3\Sigma^-$ band of CNN is shown in Fig. 3(a) with peak positions and assignments listed in Table I. These photofragment yield (PFY) spectra are a convolution of absorption and dissociation cross sections. The laser fluences were typically 200 mJ/cm^2 for photon energies between 23 500–24 200 (i.e., peaks A–C) and 80 mJ/cm^2 from 24 700–26 000 cm^{-1} (remainder of spectrum). A broad feature with a width of ≈ 100 cm^{-1} is observed near 23 850 cm^{-1} (A) in good agreement with the rotationally resolved origin band observed by Curtis *et al.*[14] Weaker features, B and C, observed 200 and 300 cm^{-1} to the blue of the origin are most likely due to sequence bands involving vibrationally excited levels of the ground state. As discussed below, peak A results from two-photon dissociation, which is why such high laser fluence was needed.

A weak feature D is observed at 24 810 cm^{-1} while prominent features E and F occur at 25 044 and 25 236 cm^{-1}, respectively; for the latter two and other features with multiplet structure, the wave number values refer to the most intense peak. Feature F shows a linear relationship between fragment intensity and laser fluence for laser fluences <30 mJ/cm^2, while saturation was seen at higher laser fluence. Expanded views of transitions E and F (scanned with laser

TABLE I. Peak positions, transition energies (cm^{-1}), and assignments of the $\tilde{A}\,^3\Pi \leftarrow \tilde{X}\,^3\Sigma^-$ PFY specturm. Assignments and frequencies from previous LIF studies are shown for comparison.

Peak	Transition Energy (cm^{-1})	Frequency (cm^{-1}) This work	LIF[a]	Assignment
A	23 850	⋯	⋯	000–000
			92	010–010 (Σ^+–Π)
			145[b]	010–010 (Δ–Π)
B	24 047	197		⋯
			196	02^-0–020 (Π–Σ^-,Δ)
C	24 157	307		020–020 (Φ–Δ)
D	24 810	960	982	02^-0–000 (Π–Σ^-)
E	25 044	1194	1098	02^+0–000 (Π–Σ^-)
F	25 236	1386	1322	100–000
G	25 592	1742		⋯
			1807	001–000
H	25 805	1955		⋯

[a]Unless otherwise denoted, all LIF frequencies are from Bondybey *et al.* (Ref. 11).
[b]Based on a reported sequence band from the gas-phase LIF study of Curtis *et al.* (Ref. 14).

fluences < 30 mJ/cm^2) are shown in Fig. 3(b), displaying significantly different rotational contours. Feature F displays three prominent subbands with a spacing of ≈ 27 cm^{-1} and a broader peak between the first two of these. The subband spacing of 27 cm^{-1} is close to the spin–orbit splitting, $A = -26.5$ cm^{-1} reported for the 000–000 band observed at lower energy in the experiments of Curtis *et al.*[14] The most intense subband possesses a width of about 1.5 cm^{-1}. Feature E, in contrast, does not possess any obvious subband structure; it consists of a peak at 25 044 cm^{-1} that is 3 cm^{-1} wide and a smaller feature ≈ 11 cm^{-1} to the red. Features G and H located above 25 300 cm^{-1} exhibit broader features. Feature H displays doublet structure with a splitting of ≈ 12 cm^{-1} and widths of 7 cm^{-1}.

B. Photofragment yield spectra, $\tilde{B}\,^3\Sigma^- \leftarrow \tilde{X}\,^3\Sigma^-$ transitions

Higher energy dissociative transitions are observed from 40 000–46 000 cm^{-1}, Fig. 4; laser fluences of ≈ 15 mJ/cm^2 were used in these measurements. The PFY spectrum shows strong, broad transitions with widths of ≈ 300 cm^{-1}. Two major progressions with spacings of ≈ 1000 cm^{-1} are observed, in agreement with the absorption bands previously observed in the matrix studies of Jacox[12] and assigned to the $\tilde{B}\,^3\Sigma^- \leftarrow \tilde{X}\,^3\Sigma^-$ band. Our gas-phase transitions are shifted by ~ 85 cm^{-1} to the blue of the Ar matrix work. The most prominent progression in our spectrum originates at 40 985 cm^{-1}, and, following the work of Jacox, is assigned to the symmetric stretch 1_0^n mode. Despite extensive scanning, we were not able to detect a weak transition near 40 000 cm^{-1} reported by Jacox. A second progression begins at 43 450 cm^{-1} and also displays a peak spacing of ~ 1000 cm^{-1}. The separation between this progression and the 1_0^n progression is 447 cm^{-1}. Since the ground state is linear and the excited state is predicted to be linear by Walsh's rules, the bend mode is not expected to be active. This second progression is most easily assigned to a combination band involving the symmetric (ν_1) and one quanta of asymmetric (ν_3) stretch with $\omega_3' = 1455$ cm^{-1}, in good agreement with the value of 1450 cm^{-1} reported by Jacox.[12]

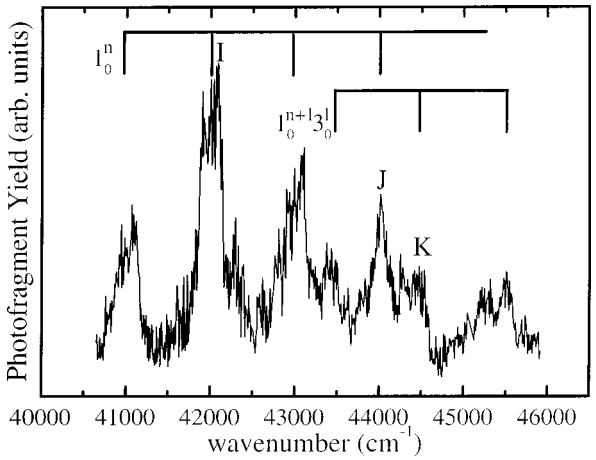

FIG. 4. Photofragment yield spectrum of the $\tilde{B}\,^3\Sigma^- \leftarrow \tilde{X}\,^3\Sigma^-$ spectrum. The 1_0^n and $1_0^{n+1}3_0^1$ progressions are indicated by the vibrational combs. Features I, J, and K denote the transitions for which translational energy distributions have been obtained.

C. Mass distributions

At the photon energies employed in this study, multiple photodissociation product channels are available. The heats of reaction (at 0 K) for energetically available product channels are shown below. $\Delta_{rxn}H_0$ for channel I (equivalent to the bond dissociation energy D_0) is determined directly in this work. The higher energy reaction channels are based upon our experimental value for D_0, JANAF thermochemical tables[30] for the heats of formation of C, N, and N_2, and the heat of formation for CN determined by Huang *et al.*:[31]

$$\mathrm{CNN}(\tilde{X}\,^3\Sigma^-) \xrightarrow{h\nu} \mathrm{N_2}(X\,^3\Sigma^-) + \mathrm{C}(^3P)$$
$$\Delta_{rxn}H_0 = 1.219 \pm 0.050 \text{ eV} \quad \text{(I)},$$
$$\mathrm{N_2}(X\,^1\Sigma_g^+) + \mathrm{C}(^1D)$$
$$\Delta_{rxn}H_0 = 2.479 \pm 0.050 \text{ eV} \quad \text{(II)},$$
$$\mathrm{CN}(X\,^2\Sigma^+) + \mathrm{N}(^4S)$$
$$\Delta_{rxn}H_0 = 3.233 \pm 0.050 \text{ eV} \quad \text{(III)},$$
$$\mathrm{N_2}(X\,^1\Sigma_g^+) + \mathrm{C}(^1S)$$
$$\Delta_{rxn}H_0 = 3.903 \pm 0.050 \text{ eV} \quad \text{(IV)},$$
$$\mathrm{CN}(A\,^2\Pi) + \mathrm{N}(^4S)$$
$$\Delta_{rxn}H_0 = 4.379 \pm 0.050 \text{ eV} \quad \text{(V)},$$
$$\mathrm{CN}(X\,^2\Sigma^+) + \mathrm{N}(^2D)$$
$$\Delta_{rxn}H_0 = 5.616 \pm 0.050 \text{ eV} \quad \text{(VI)}.$$

The upper states accessed in the $\tilde{A}\,^3\Pi \leftarrow \tilde{X}\,^3\Sigma^-$ transitions in Fig. 3 can only dissociate to channels I and II and the expected 12:28 photofragment mass ratio is observed. The higher energy $\tilde{B}\,^3\Sigma^- \leftarrow \tilde{X}\,^3\Sigma^-$ transitions between 5.1–6.0 eV have multiple dissociation pathways available. We have examined the mass distributions as a function of translational energy both above and below the thermodynamic limits for

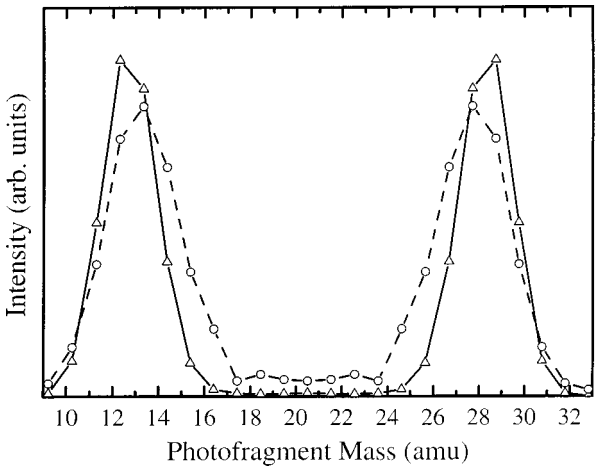

FIG. 5. Photofragment mass distributions for transition *K* of the $\tilde{B}\,^3\Sigma^- \leftarrow \tilde{X}\,^3\Sigma^-$ band for translational energies >1 eV (triangles) and <0.8 eV (circles). For low translational energies, the mass of the light (heavy) fragment shows a shift to higher (lower) masses.

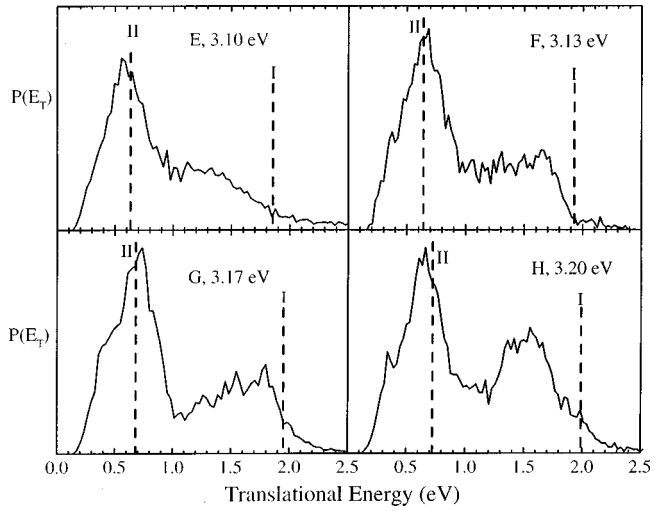

FIG. 6. Translational energy distributions for $\tilde{A}\,^3\Pi \leftarrow \tilde{X}\,^3\Sigma^-$ band transitions E–G. The photon energies for each transition is given and the maximum translational energies for channels I and II derived from transition F are indicated with the dashed vertical lines.

the CN+N channels III and V; examples are shown in Fig. 5 for transition K. At translational energies >2.5 eV, only channels I and II are accessible and the expected 12:28 mass ratio is observed. At translational energies > 1 eV the mass ratio continues to be 12:28 for all transitions in the $\tilde{B}\,^3\Sigma^- \leftarrow \tilde{X}\,^3\Sigma^-$ band. For transitions J and K in Fig. 4, the mass distributions broaden considerably at translational energies < 0.8 eV (circles in Fig. 5) and a slight shift to higher (lower) mass is observed for the light (heavy) photofragment, indicating that the N+CN mass channel contributes.

D. Translational energy and angular distributions

The coincident detection scheme measures both the energy and angular distributions of the photofragments. The two-dimensional coupled translational energy distribution, $P(E_T,\theta)$ can be separated into the angle-independent translational energy distribution $P(E_T)$ and the energy-dependent anisotropy parameter $\beta(E_T)$ which describes the angular distribution of the fragments

$$P(E_T,\theta)=P(E_T)[1+\beta(E_T)P_2(\cos\theta)]. \quad (1)$$

The anisotropy parameter β ranges from +2 to −1, corresponding to $\cos^2\theta$ and $\sin^2\theta$ angular distributions, respectively.

1. $\tilde{A}\,^3\Pi \leftarrow \tilde{X}\,^3\Sigma^-$ $P(E_T)$ distributions

The $P(E_T)$ distributions for peaks E, F, G, and H of the $\tilde{A}\,^3\Pi \leftarrow \tilde{X}\,^3\Sigma^-$ band are shown in Fig. 6. We will comment on the $P(E_T)$ distribution for the origin band (peak A) in Sec. III D 3. The $P(E_T)$ distributions display bimodal distributions with a high energy component that extends toward ≈2 eV and a low energy feature peaked at 0.6 eV. The relative intensity of the higher energy component increases with larger photon energies. The $P(E_T)$ distribution for the 100–000 transition shows a sharp onset in signal at 1.91 eV, defining the maximum translational energy, $E_T^{\max}$. The other $\tilde{A}\,^3\Pi \leftarrow \tilde{X}\,^3\Sigma^-$ transitions do not display such sharp onsets and instead show a gradual decrease in signal towards higher translational energies.

2. $\tilde{B}\,^3\Sigma^- \leftarrow \tilde{X}\,^3\Sigma^-$ $P(E_T)$ distributions

$P(E_T)$ distributions for three $\tilde{B}\,^3\Sigma^- \leftarrow \tilde{X}\,^3\Sigma^-$ transitions are shown in Fig. 7. Figures 7(a)–7(c) (peaks I, J, and K) correspond to $P(E_T)$ distributions for events analyzed as producing $C+N_2$ photofragments while Fig. 7(d) (peak J) corresponds to N+CN events. As discussed in Sec. III C and shown in Fig. 5, these two mass channels are incompletely resolved in our experiment. As a consequence, Figs. 7(b) and 7(d) obtained at the same photon energy are similar, the main

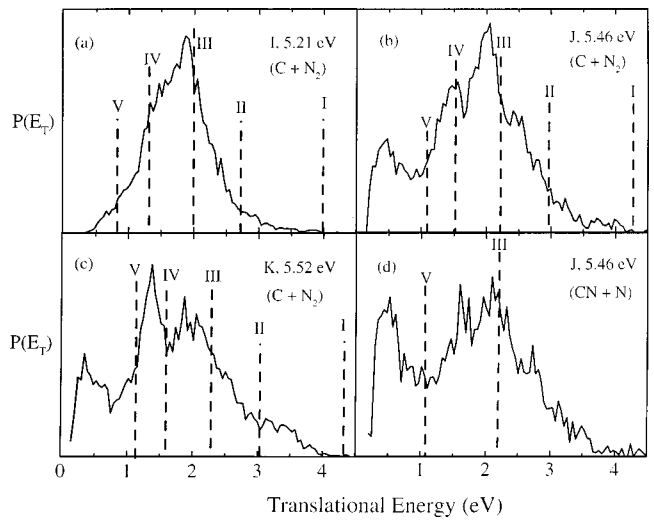

FIG. 7. Translational energy distributions for the $\tilde{B}\,^3\Sigma^- \leftarrow \tilde{X}\,^3\Sigma^-$ transitions. The distributions for $C+N_2$ products for transitions I, J, and K are shown in (a), (b), and (c), respectively. The transition photon energies are indicated and the maximum translational energy ($E_T^{\max}$) for product channels I–V are denoted by vertical dashed lines. The distribution for N+CN products for transition J is shown in (d).

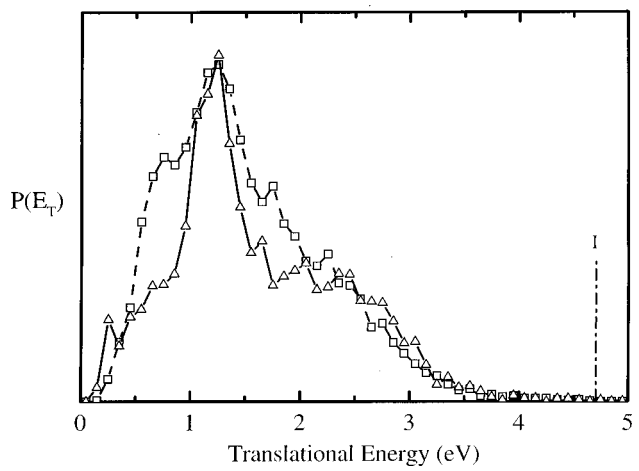

FIG. 8. $P(E_T)$ distributions for photon energies of 2.955 eV (□), corresponding to the $\tilde{A}\,^3\Pi \leftarrow \tilde{X}\,^3\Sigma^-$ origin, and 5.91 eV (△).

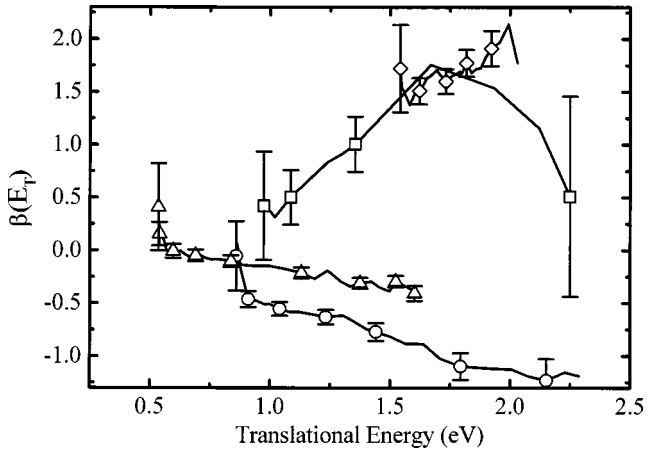

FIG. 9. Photofragment anisotropy parameter, β, as a function of translational energy for peak G in the $\tilde{A}\,^3\Pi \leftarrow \tilde{X}\,^3\Sigma^-$(△), the $\tilde{B}\,^3\Sigma^- \leftarrow \tilde{X}\,^3\Sigma^-(400-000)$ transition (◇), the 5.91 eV transition (□), and the 2.955 eV two-photon transition (○).

difference being that the broad peak at $E_T = 0.5$ eV, which only appears when transitions J or K are excited, is considerably enhanced relative to the signal above 1 eV in Fig. 7(d). The signal above 1 eV in Fig. 7 is entirely from $C+N_2$ since the mass spectrum of the fragments is identical to that obtained at lower photon energies where this is the only channel available (Fig. 5), whereas the peak around 0.5 eV is attributed to N+CN because of its enhancement in Fig. 7(d). The latter assignment is again consistent with the photofragment mass spectra in Fig. 5.

The observed structure for the $C+N_2$ mass channel, with features between 0.5 to 1.0 eV in width, is much too broad to attribute to individual vibrational states of the N_2 products. Furthermore, the sharp rises do not exactly coincide with the thermodynamic thresholds for various product states and do not shift with excitation energy, making the assignment of the product channel ambiguous. The internal energy distribution appears to depend both upon excitation energy as well as the vibronic character of the transition. The $P(E_T)$ distributions for transitions J and K show more signal above 3 eV than transition I and a peak near 1.5 eV not seen from transition I (the feature at 0.5 eV is from N+CN products, as discussed above). Although $K(1_0^n 3_0^1)$ is only 60 meV higher in energy than $J(1_0^n)$, the $P(E_T)$ distribution for K peaks sharply near 1.4 eV as opposed to 2.0 eV for J, suggesting that excitation of the asymmetric stretch leads to increased internal excitation of the photofragments.

3. $P(E_T)$ distributions from the origin and higher energy transitions

The $P(E_T)$ distribution for the origin transition at 2.955 eV, Fig. 8, reveals a broad distribution peaked near 1.3 eV extending to 4.7 eV, which is 1.75 eV higher in energy than the initial photon energy. Gas phase kinetic data[13] and *ab initio* calculations[15,20,32] indicate that the CNN radical is thermodynamically stable with respect to the lowest energy dissociation asymptote. The high translational energy fragments must therefore be produced via a multiphoton process. The $P(E_T)$ distribution resulting from excitation with a single photon at 5.91 eV (i.e., 2×2.955 eV) is also shown in Fig. 9. Due to the low laser fluence (≈ 3 mJ/cm^2) and small absorption cross section at the higher photon energy, this data set consists of approximately 1/10 the number of data points as the $P(E_T)$ distribution at 2.955 eV. Even with these poor statistics, similarities between the two data sets are readily apparent, both showing broad distributions peaking near 1.3 eV and extending towards higher translational energies. The similarity in $P(E_T)$ distributions suggests the distribution at lower photon energy results from two-photon absorption, and that not only the total energy but also the final excited state is the same for both processes.

4. Angular distributions

Photofragment anisotropy parameters $\beta(E_T)$ for representative $\tilde{A}\,^3\Pi \leftarrow \tilde{X}\,^3\Sigma^-$ and $\tilde{B}\,^3\Sigma^- \leftarrow \tilde{X}\,^3\Sigma^-$ transitions as well as one-photon and two-photon transitions with total excitation energy of 5.91 eV are shown in Fig. 9. Angular distributions for the $\tilde{A}\,^3\Pi \leftarrow \tilde{X}\,^3\Sigma^-$ band are essentially isotropic with $\beta \approx 0$ at translational energies less than 1 eV and become increasingly anisotropic at higher translational energies with $\beta = -0.2$ at 1.5 eV. The photofragment anisotropies for the $\tilde{B}\,^3\Sigma^- \leftarrow \tilde{X}\,^3\Sigma^-$ transitions are significantly more anisotropic showing positive β parameters which peak near 2. Although the $P(E_T)$ distributions in Fig. 8 at photon energies of 2.955 and 5.91 eV are similar, the photofragment angular distributions are quite different. Excitation at 5.91 eV results in a positive β parameter at all translational energies, whereas excitation at 2.955 eV yields a negative β parameter reaching its limit of -1 for $E_T > 1.7$ eV.

IV. ANALYSIS

A. Photofragment yield spectra

With the aid of previous gas-phase[14] and matrix[6,11] LIF studies, we have been able to assign several vibronic features of the $\tilde{A}\,^3\Pi \leftarrow \tilde{X}\,^3\Sigma^-$. PFY spectra are a convolution of both absorption and dissociation and may therefore exhibit different structure than emission or absorption-based techniques.

Perturbations due to the matrix environment must also be considered when comparing our gas-phase studies with matrix results.

Feature A, centered near 23 840 cm^{-1}, agrees well with the gas phase LIF excitation spectrum of the $\tilde{A}\,^3\Pi \leftarrow \tilde{X}\,^3\Sigma^-$ origin by Curtis *et al.*[14] with a reported term energy of 23 850 cm^{-1}. The band contour of this feature in our PFY spectrum does not show the resolved fine structure seen in the gas phase LIF spectrum. At the high fluence needed to observe PFY signal, $\approx$200 mJ/cm^2, saturation effects and power broadening of individual lines are likely.

Since feature A in the PFY spectrum does not display resolved structure, a determination of the term energy for the $\tilde{A}\,^3\Pi \leftarrow \tilde{X}\,^3\Sigma^-$ band is not obvious and we adopt the value of 23 850 cm^{-1} from Curtis *et al.* Excitation energies for the other transitions within the $\tilde{A}$ state manifold are shown in Table I along with matrix LIF results. Curtis *et al.* have reported a weak band 145 cm^{-1} to the blue of the origin with analogous subband structure; this has been tentatively assigned to the $(010-010)\Delta \leftarrow \Pi$ sequence band, yielding a gas-phase bend frequency of 540 cm^{-1} for the $\tilde{A}\,^3\Pi$ state.[33] Our PFY spectrum exhibits broad dissociation signal 145 cm^{-1} above the origin along with more intense features B and C located $\approx$200 and 300 cm^{-1} above the origin. Feature C can be reasonably assigned to the $(020-020)\Phi \leftarrow \Delta$ transition, while the assignment of feature B is less certain.

We next consider the higher-lying features. Transition F shows prominent features with subband spacing of about 27 cm^{-1} and a broader peak between the first two of these. The three evenly spaced subbands are assigned to the $^3\Pi_2$, $^3\Pi_1$, and $^3\Pi_0$ Q-type bandheads of the $\tilde{A}\,^3\Pi \leftarrow \tilde{X}\,^3\Sigma^-$ transition. The appearance of this fine structure in the PFY spectrum is quite different than in the origin band observed by Curtis *et al.*[14] However, their experiment reports a rotational temperature of 500 K as opposed to 50 K in our experiment. Using the same structural parameters used previously by Curtis *et al.* to simulate their spectrum but assuming a rotational temperature of 50 K, we generate the three equally-spaced subbands associated with transition F. The subband structure and vibrational frequency of 1387 cm^{-1} are consistent with an assignment of F to the 100–000 transition, although the gas-phase transition occurs 64 cm^{-1} to the blue of the corresponding matrix LIF transition (see Table I).

The matrix LIF spectrum[11] shows two features with energies similar to D and E in the PFY spectrum that were assigned to transitions to the lower (02^-0) and upper (02^+0) Renner–Teller states, and these assignments appear reasonable for peaks D and E as well. The Renner–Teller interaction commonly reduces the spin–orbit splitting as has been observed previously in CCO.[34] The lack of subband structure associated with feature E supports its assignment to a Renner–Teller state. Peak D lies 20 cm^{-1} below the corresponding matrix transition, while E is 100 cm^{-1} higher, indicating a strong matrix effect. In their matrix studies, Bondybey and English determined the Renner parameter $\epsilon\omega_2$ to be -36.75 cm^{-1}, significantly less than the gas-phase values of -104.4 and -91.1 cm^{-1} for the isoelectronic species CCO (Refs. 34, 35) and NCN.[36] Assigning transitions D and E to the 02^-0 and 02^+0 states, respectively, we derive $\omega_2' = 539\,cm^{-1}$, in good agreement with the value estimated from the work of Curtis *et al.*,[14] and a Renner value $\epsilon = -0.154$ yielding $\epsilon\omega_2 = -83\,cm^{-1}$, in much better agreement with the other isoelectronic species. The large discrepancy between the gas-phase and matrix values is surprising. However, the spin–orbit parameter, A was found to be -9 and -26.5 cm^{-1}, respectively for matrix[11] and gas-phase[14] measurements on CNN, indicating that the matrix substantially perturbs the electronic coupling to the internuclear axis.

The relative intensities of the Renner–Teller features D and E are reversed in the matrix LIF and PFY spectra. In the absence of other perturbations, we expect the intensity for the two 020 Π states to be approximately equal. The intensity of the lower Renner–Teller state in LIF matrix measurements[11] is more than four times that of the upper Renner–Teller state, whereas our PFY measurements show the 02^+0 transition to be at least five times more intense than the 02^-0 band. These observations suggest that the lower Renner–Teller state decays primarily via emission, whereas the upper Renner–Teller component has a significantly higher quantum yield for dissociation, thereby depleting the LIF signal associated with this peak.

Higher energy features G and H are observed 1742 cm^{-1} and 1967 cm^{-1} above the origin. These features do not display clear subband structure nor do they agree well with reported LIF matrix transitions. Feature G could be the transition to the 001 level, although this implies a gas-phase frequency shift of -65 cm^{-1} from the matrix value of 1807 cm^{-1}. Transition H is tentatively assigned to the 04^-0-000 transition, as its excitation energy is about twice that of peak D. Other possible assignments include combination band transitions originating from vibrationally excited levels of the ground state.

All of the vibronic transitions of the $\tilde{A}\,^3\Pi \leftarrow \tilde{X}\,^3\Sigma^-$ band deviate to some extent from the LIF matrix studies, suggesting substantial host–guest interactions exist for CNN. Analogous shifts between matrix and gas phase frequencies were observed previously by Bondybey and English[37] for the $\tilde{A}\,^2\Delta$ state of the CCN radical in solid Ar.

The agreement between the gas-phase measurements and matrix values for the $\tilde{B}\,^3\Sigma^- \leftarrow \tilde{X}\,^3\Sigma^-$ transitions appear to be much closer than for the $\tilde{A}\,^3\Pi \leftarrow \tilde{X}\,^3\Sigma^-$ band. The 1_0^n and $1_0^n 3_0^1$ progressions yield values of $\nu_1 \approx 1000\,cm^{-1}$ and $\nu_3 \approx 1455\,cm^{-1}$, in good agreement with the matrix studies of Jacox.[12] The extended progressions are indicative of a large change in geometry between the $\tilde{X}\,^3\Sigma^-$ and $\tilde{B}\,^3\Sigma^-$ states; consistent with the promotion of an electron from a bonding π orbital to a non/antibonding π^* orbital. The broad resonances indicate lifetime broadening due to rapid predissociation.

B. Translational energy distributions

1. $\tilde{A}\,^3\Pi \leftarrow \tilde{X}\,^3\Sigma^-$ transitions

The $P(E_T)$ distributions in Fig. 6 and 7 demonstrate how available energy is distributed between the photofragments. Energy balance for CNN photodissociation to N_2+C is described by Eq. (2):

$$h\nu + E_{\text{int}}(\text{CNN}) + E_{\text{elec}}(\text{CNN}) = D_0(\text{CNN}) + E_T + E_v(\text{N}_2) + E_R(\text{N}_2) + E_{\text{elec}}(\text{C}), \quad (2)$$

where $h\nu$ is the photon energy, $E_{\text{int}}(\text{CNN})$ is the average rotational energy of the parent radical, $E_{\text{elec}}(\text{CNN})$ is the initial electronic state of the radical, D_0 is the dissociation energy, E_T is the measured translational energy, $E_v(\text{N}_2)$ and $E_R(\text{N}_2)$ are the N_2 vibrational and rotational energies, respectively, and $E_{\text{elec}}(\text{C})$ is the atomic state of carbon. An analogous equation can be written for the CN+N channel. The parent rotational temperature of 50 K yields $E_{\text{int}}(\text{CNN}) \approx 33\ \text{cm}^{-1}$. $D_0(\text{CNN})$ for the N_2 loss channel can be extracted from these distributions by determining $E_T^{\max}$, the translational energy corresponding to photofragments with zero internal energy. In the $\tilde{A}\,^3\Pi \leftarrow \tilde{X}\,^3\Sigma^-$ band, a sharp threshold for dissociation signal is observed for the 100–000 transition (F), yielding a dissociation energy, $D_0 = 1.22 \pm 0.05$ eV.

The translational energy distributions for the other transitions in Fig. 6 do not show as sharp a threshold, and G and H in particular clearly extend beyond the maximum E_T implied by the above dissociation energy. However, the distributions for E, G, and H energies were measured at laser fluences ~80 mJ/cm^2 compared with 30 mJ/cm^2 for F, and may reflect multiphoton absorption. Furthermore, the assignments of transitions G and H are uncertain and may involve excitation from vibrationally excited levels of the ground state, giving rise to higher translational energy signal than would be expected from transitions originating from the (000) level of the $\tilde{X}\,^3\Sigma^-$ state.

Using Eq. (3), we determine $\Delta_f H_0(\text{CNN}) = 6.16 \pm 0.05$ eV from our experimental value for D_0 and JANAF thermochemical tables for the heats of formation of C and N_2.[30]

$$\Delta_f H_0(\text{CNN}) = \Delta_f H_0(\text{C}(^3P)) + \Delta_f H_0(\text{N}_2(X\,^1\Sigma_g^+)) - D_0. \quad (3)$$

This value is more precise than previous values of 6.6 ± 1.0 eV and 5.9 ± 0.2 eV reported by Gurvich[16] and Clifford *et al.*,[15] respectively. The uncertainty in our value for the heat of formation for CNN is considerably less since the thermochemical cycle employed in this study is linked to the photofragments $\text{C}(^3P)$ and $\text{N}_2(X\,^1\Sigma_g^+)$ whose heats of formation are extremely well-known. Our heat of formation is just outside the error bars of the value derived from recent photoelectron and proton affinity measurements of Clifford *et al*. However, the value obtained by Clifford *et al.* involves a thermochemical cycle referenced to $\Delta_r H_0(\text{H}_2\text{CNN})$ for which the authors adopt a value of 2.85 eV based upon *ab initio* calculations, and this may be the cause of the discrepancy. Experimental[13,38–42] and theoretical[15,43–47] values for the heat of formation of diazomethane (H_2CNN) vary from 2.2–3.3 eV.

Using our $\Delta_f H_0(\text{CNN})$, ground state frequencies from IR matrix studies,[6] and tabulated values for N_2 and C,[30] we determine $\Delta_f H_{298}(\text{CNN}) = 6.15 \pm 0.05$ eV. Our experimental results coupled with $D_0(\text{RH})$ and $D_{298}(\text{RH})$ values from Clifford *et al.* yield the following heats of formation: $\Delta_f H_0(\text{HCNN}) = 5.02 \pm 0.18$ eV, $\Delta_f H_{298}(\text{HCNN}) = 4.98 \pm 0.18$ eV, $\Delta_f H_0(\text{H}_2\text{CNN}) = 3.09 \pm 0.21$ eV, and $\Delta_f H_{298}(\text{H}_2\text{CNN}) = 3.03 \pm 0.21$ eV. These values for the heat of formation of diazomethane are in excellent agreement with the experimental value, $\Delta_f H_{298}(\text{H}_2\text{CNN}) = 3.07 \pm 0.21$ eV, reported by Hassler and Setser[41] and theoretical values, $\Delta_f H_0(\text{H}_2\text{CNN}) = 3.09$ eV (Ref. 44) and 3.06 eV,[47] based upon *ab initio* calculations of $D_0(\text{CH}_2\text{-N}_2)$.

In addition to yielding an accurate heat of formation, the $P(E_T)$ distributions provide detailed information regarding the nature and extent of photofragment excitation and hence provide considerable insight into the dissociation mechanism. The distributions do not exhibit well-resolved vibrational structure of the N_2 fragment. The N_2 vibrational frequency is considerably larger than our energy resolution, and we would easily observe N_2 vibrational structure in the $P(E_T)$ distributions if the N_2 were rotationally cold, as was the case for NCN photodissociation.[21] The absence of such structure thus indicates that the N_2 is formed with a broad rotational energy distribution, the width of which is at least at large as the N_2 vibrational frequency ($\omega_e = 2358\ \text{cm}^{-1}$) corresponding to $J \approx 35$. Assuming a single Boltzmann rotational distribution for each vibrational feature and an instrument resolution of 30 meV, resolved vibrational structure of the N_2 fragment should be observed for rotational distributions which peak at J values less than 50 quanta ($T_{\text{rot}} \approx 15\,000$ K). Hence, the actual N_2 rotational distribution must be hotter than this.

The bimodal $P(E_T)$ distributions suggest that two distinct dissociation pathways are present yielding different product state distributions. One explanation for two different distributions would be the presence of two different product channels [e.g., $\text{C}(^3P)$ and $\text{C}(^1D)$ products]. However, this does not appear to be the case. $E_T^{\max}$ for the $\text{C}(^1D) + \text{N}_2$ channel is indicated by the dot-dashed line in Fig. 6. In all four $P(E_T)$ distributions the lower energy component begins at translational energies ⩾200 meV than this value of $E_T^{\max}$, suggesting it is not due to $\text{C}(^1D) + \text{N}_2$. The low energy feature thus appears to be $\text{C}(^3P)$ plus highly internally excited N_2.

2. $\tilde{B}\,^3\Pi \leftarrow \tilde{X}\,^3\Sigma^-$ transitions

The $P(E_T)$ distributions for the $\tilde{B}\,^3\Sigma^- \leftarrow \tilde{X}\,^3\Sigma^-$ transitions in Fig. 7 all peak at translational energies well below the maximum for ground state $\text{C}(^3P)$ products. While multiple product channels are energetically accessible, our product mass distributions suggest that the $\text{C} + \text{N}_2$ products are the dominant photolysis products. Transition K, a member of the $1_0^n 3_0^1$ progression, produces significantly more internal energy into the products than the nearby transition J of the 1_0^n progression suggesting that a mode-specific mechanism may be involved with excitation of the asymmetric stretch leading to additional excitation of the N_2 photofragment. The energy separation of the structured features in the $P(E_T)$ distributions for transitions J and K is much too large to attribute to vibrational structure of the N_2 photofragment.

The calculated maximum translational energies for channel I–V, based upon our experimentally determined value for D_0, are indicated in Fig. 7 with vertically dashed lines. It is

tempting to assign the various structured features to new dissociation channels. The features at 1.87 and 2.05 eV for transitions I and J appear to correspond to the opening of channel III. However, our mass ratio of 12:28 indicates that CN+N products are not formed at this translational energy and that these features must be due to internally excited $C+N_2$ products. A new feature appears to grow in for transition K peaking at 1.4 eV and the onset of this feature corresponds energetically with the opening of the spin-forbidden $C(^1S)$ channel. However, the broad resonances in the PFY spectra suggest that the $\tilde{B}\,^3\Sigma^-$ state decays on an ~100 fs time scale, making an intersystem crossing mechanism less likely. We therefore propose that this feature at 1.4 eV for transition K does not correspond to $C(^1S)$ products, but to vibrationally and rotationally excited $C(^3P)$ products.

Finally, low energy features near 0.5 eV are observed for transitions J and K. Our photofragment mass distributions in Fig. 5 and $P(E_T)$ distribution for transition J in Figs. 7(b) and 7(d) indicate that this low energy feature is due to CN+N products. Due to its appearance at low translational energy (<1 eV), we attribute this feature to $CN(A\,^2\Pi)+N(^4S)$ products. Our results do not show any evidence for the ground state $CN(X\,^2\Sigma^+)+N(^4S)$ channel, but we cannot rule it out as a minor channel contributing to the $P(E_T)$ distributions at higher E_T.

The photofragment anisotropy resulting from the $\tilde{B}\,^3\Sigma^-\leftarrow\tilde{X}\,^3\Sigma^-$ transitions are significantly more anisotropic than the $\tilde{A}\,^3\Pi\leftarrow\tilde{X}\,^3\Sigma^-$ transitions with β values close to the limiting value of +2 for a parallel transition dipole moment. This suggests rapid dissociation, a result consistent with the broad peaks seen in the PFY spectrum.

3. Origin and higher energy transitions

As discussed earlier, the signal at high E_T observed for the $P(E_T)$ distribution at 2.955 eV (Fig. 8) is indicative of two-photon dissociation. The PFY spectrum at this photon energy shows a resonance corresponding to the $\tilde{A}\,^3\Pi\leftarrow\tilde{X}\,^3\Sigma^-$ (000–000) transition, indicating that the origin is an intermediate resonant state in the two-photon dissociation. It is of interest to determine the final state from which the radical dissociates. Matrix work by Jacox[4] has shown that the $\tilde{B}\,^3\Sigma^-\leftarrow\tilde{X}\,^3\Sigma^-$ band progression in an Ar matrix extends to 47 619 cm^{-1}(5.90 eV) and a band assigned to a different electronic state with proposed $^3\Pi$ symmetry is observed at 48 543 cm^{-1}(6.02 eV) and 49 116 cm^{-1}(6.08 eV) in Ar and N_2 matrices, respectively. The electronic configurations for these states (Sec. I) show that both the $\tilde{B}\,\Sigma^-\leftarrow\tilde{A}\,^3\Pi$ and $^3\Pi\leftarrow A\,^3\Pi$ transitions are allowed. The $P(E_T)$ distribution obtained at an energy of 5.91 eV displays very similar structure to the 2.955 eV two-photon $P(E_T)$ distribution suggesting that the same excited state is accessed. The photofragment signal at 5.91 eV was found to be particularly weak, <1/8 of the signal of transition I, suggesting that at this energy, we do not access the strong absorption associated with the $^3\Pi$ state, but rather the blue edge of the $\tilde{B}\,^3\Sigma^-$ state.

Further insight is obtained from the photofragment angular distributions (Fig. 9). The anisotropy parameter for the single-photon process at 5.91 eV approaches $\beta=+2$, indicating rapid dissociation via a final state of $^3\Sigma^-$ symmetry, presumably the $\tilde{B}\,^3\Sigma^-$ state. In contrast, the two-photon process yields negative β parameters at all E_T. Initial excitation of the $\tilde{A}\,^3\Pi\leftarrow\tilde{X}\,^3\Sigma^-$ band should in principle form aligned CNN radicals which are then dissociated by the absorption of a second photon, possibly leading to higher-order terms in the angular distribution.[48,49] Nevertheless, the angular distribution is reasonably described by Eq. (1), with β approaching its limiting value of −1 at translational energies >1.7 eV. We interpret this to mean that the lifetime of the $\tilde{A}\,^3\Pi$ state origin (>200 ns) is sufficiently long so that alignment is significantly reduced prior to absorption of the second photon, and that the negative anisotropy parameter reflects a perpendicular transition from the intermediate $\tilde{A}\,^3\Pi$ state to a rapidly dissociating upper state. This is consistent with assigning the second photon absorption to excitation of the $\tilde{B}\,^3\Sigma^-\leftarrow\tilde{A}\,^3\Pi$ band.

V. DISCUSSION

The photofragment yield spectra, translational energy, and angular distributions show that the CNN radical undergoes complicated dissociation dynamics. In this section selected aspects of these dynamics are discussed in more detail.

Previous LIF spectra[11] and our PFY spectra provide complementary information on the excited state dynamics of the CNN radical. The measured fluorescence lifetime of 220 ns for the $\tilde{A}\,^3\Pi$ state origin agrees well with the calculated value of 216 ns,[32] suggesting that this state does not undergo any radiationless processes. Since the $\tilde{A}\,^3\Pi$ state lies more than 1.73 eV above the lowest dissociation asymptote, these results imply a barrier to dissociation for the $\tilde{A}\,^3\Pi$ state. Our results concur, demonstrating that photofragments generated at the excitation energy of the $\tilde{A}\,^3\Pi\leftarrow\tilde{X}\,^3\Sigma^-$ origin are produced from a resonant two-photon process. Peak E, assigned to the 02^+0-000 transition and located ≈1200 cm^{-1} above the origin, does undergo rapid one-photon dissociation, whereas comparison of the LIF and PFY spectra indicates that fluorescence competes effectively with dissociation from the lower-lying 02^-0 state. A simple explanation of these results is the presence of a barrier located 960–1200 cm^{-1} above the origin, inhibiting dissociation from the 02^-0 state but not the 02^+0 state.

The absence of vibrational structure in the $P(E_T)$ distributions from the $\tilde{A}\,^3\Pi\leftarrow\tilde{X}\,^3\Sigma^-$ and $\tilde{B}\,^3\Sigma^-\leftarrow\tilde{X}\,^3\Sigma^-$ transitions and the implied high level of N_2 rotational excitation is surprising given that the ground and excited states are linear. It appears that dissociation proceeds through bent transition states that exert substantial torque on the N_2 fragment. Extensive rotational excitation of the molecular fragment has been observed by Continetti *et al.*[22] in the photodissociation of N_3 from the linear $\tilde{B}\,^2\Sigma_u^+$ state, leading these authors to conclude that the dissociation mechanism involves bent geometries. In our recent photodissociation studies of the structural isomer NCN,[21] molecular nitrogen was also found to be the dominant product channel. However, unlike the CNN

radical, the translational energy distributions from NCN revealed well-resolved vibrational structure of the N_2 photofragment with fragment rotational distributions that peak between $J=20-35$. This relatively low level rotational excitation supports a symmetric, cyclic transition state for NCN photodissociation which can fall apart to $C+N_2$ without applying much torque to the molecular fragment.

The isoelectronic species, N_3^+ provides a useful system with which to compare the CNN radical. Friedman *et al.*[50] have observed the predissociation cross section of the $\tilde{A}\,^3\Pi_u \leftarrow \tilde{X}\,^3\Sigma_g^-$ band. No fragmentation was observed for the origin, located 0.87 eV above the $N^+(^3P)+N_2(X\,\Sigma_g^+)$ dissociation asymptote and the first assigned predissociative transition is the 020–000 band. No assignment of the upper and lower Renner components was made. Individual rotational lines for the 100–000 transition were resolved and all were found to be instrumentally narrow placing a lower limit on the excited state lifetime of >50 ps. The authors proposed that the inability of the origin to dissociate and the long lifetime of the 100–000 state is due to a barrier along the dissociation coordinate. This hypothesis is borne out by recent *ab initio* calculations by Bennett *et al.*[51] on the collinear adiabatic potential energy surfaces of N_3^+; these show a substantial barrier ($\sim$1 eV) for dissociation of the $\tilde{A}\,^3\Pi$ state to products $N^+(^3P)+N_2(\tilde{X}\,\Sigma_g^+)$ resulting from an avoided crossing between the $\tilde{A}\,^3\Pi$ state, which diabatically correlates with $N+N_2^+$ products (isoelectronic with N+CN), and a repulsive $^3\Pi$ state that correlates diabatically with lower-lying $N^+(^3P)+N_2(X\,^1\Sigma_g^-)$ products (isoelectronic with $C+N_2$). The absence of predissociation of the $\tilde{A}\,^3\Pi$ state 000 level due to a barrier along the dissociation coordinate thus occurs in both N_3^+ and CNN, suggesting that an avoided crossing also occurs in CNN.

The calculations by Bennett *et al.*[51] indicate that excited state dissociation of N_3^+ is strongly affected by nonadiabatic effects, including avoided crossings and conical intersections. For example, in addition to the avoided crossing involving the $\tilde{A}\,^3\Pi$ state in collinear geometries, this state also undergoes a conical intersection with an excited $^3\Sigma^-$ state. As a consequence, the effective barrier to dissociation is reduced if the molecule becomes nonlinear. If a similar picture can be applied to CNN dissociation, dissociation through a bent geometry may provide the lowest energy pathway to $C+N_2$ products, providing a possible explanation for the extensive rotational excitation seen in the N_2 product in our experiment. We hope that future theoretical work on both linear and nonlinear potential energy surfaces of CNN will allow for a detailed picture of the nonadiabatic processes involved in its dissociation.

VI. CONCLUSIONS

The photodissociation spectroscopy and dynamics of the $\tilde{A}\,^3\Pi$ and $\tilde{B}\,^3\Sigma^-$ states of CNN have been investigated by fast beam photofragment spectroscopy. Gas-phase predissociative resonances have been observed for the $\tilde{A}\,^3\Sigma \leftarrow \tilde{X}\,^3\Sigma^-$ band. The origin transition of this band does not dissociate, but is an intermediate state in a resonant two-photon excitation promoting the CNN radical to a high vibronic state of the $\tilde{B}\,^3\Sigma^-$ state which subsequently dissociates. Our results suggest that the $\tilde{A}\,^3\Pi$ state is subject to a barrier to dissociation approximately 1000 cm^{-1} above its vibrational ground state. PFY spectra show broad resonances for the $\tilde{B}\,^3\Sigma^- \leftarrow \tilde{X}\,^3\Sigma^-$ band providing the first gas-phase observation of this band. Product mass analysis shows that $C+N_2$ is the dominant channel, although a small amount of N+CN results from $\tilde{B}\,^3\Sigma^-$ state dissociation.

Photodissociation of the CNN radical in the $\tilde{A}\,^3\Pi$ and $\tilde{B}\,^3\Sigma^-$ states induces large rotational excitation of the N_2 product obscuring any underlying vibrational structure of the N_2 fragment, and implying that nonlinear geometries are involved in fragmentation. Further, our results show that the NCN and CNN radicals access different regions of the global $C+N_2$ potential energy surface. The former dissociates via a symmetric, cyclic structure yielding low rotational excitation, while the latter dissociates via bent transition states imparting much more torque on the recoiling N_2 fragment. Additionally, we have obtained an accurate heat of formation for the CNN radical from which we derive the heats of formation of HCNN and H_2CNN.

ACKNOWLEDGMENTS

This research is supported by the Director, Office of Energy and Research, Office of Basic Energy Sciences, Chemical Sciences Division, of the U.S. Department of Energy under Contract No. DE-AC03-76F00098. R.T.B. would like to thank Professor G. B. Ellison and Dr. E. P. Clifford for useful discussions regarding the synthesis of diazomethane and the preparation of CNN^-, A. Souers for synthetic equipment, and Professor P. J. Sarre for useful comments regarding the $\tilde{A}\,^3\Pi \leftarrow \tilde{X}\,^3\Sigma^-$ spectrum.

[1] C. P. Fenimore, in *Procedings of the Thirteenth Symposium (International) on Combustion* (The Combustion Institute, Pittsburgh, PA, 1971), p. 373.
[2] E. Wasserman, L. Barash, and W. A. Yager, J. Am. Chem. Soc. **87**, 2075 (1965).
[3] G. R. Smith and W. Weltner, Jr., J. Chem. Phys. **62**, 4592 (1975).
[4] D. E. Milligan and M. E. Jacox, J. Chem. Phys. **44**, 2850 (1966).
[5] R. L. DeKock and W. Weltner, Jr., J. Am. Chem. Soc. **93**, 7106 (1971).
[6] B. E. Wurfel, A. Thoma, R. Schlachta, and V. E. Bondybey, Chem. Phys. Lett. **190**, 119 (1992).
[7] T. D. Goldfarb and G. C. Pimentel, J. Am. Chem. Soc. **82**, 1865 (1959).
[8] G. W. Robinson and M. McCarty, Jr., J. Am. Chem. Soc. **82**, 1859 (1960).
[9] W. Weltner, Jr. and D. McLeod, Jr., J. Chem. Phys. **45**, 3096 (1966).
[10] M. Tulej, J. Fulara, A. Sobolewski, M. Jungen, and J. P. Maier, J. Chem. Phys. **112**, 3747 (2000).
[11] V. E. Bondybey and J. H. English, J. Chem. Phys. **67**, 664 (1977).
[12] M. E. Jacox, J. Mol. Spectrosc. **72**, 26 (1978).
[13] W. Braun, A. M. Bass, D. D. Davis, and J. D. Simmons, Proc. R. Soc. London, Ser. A **312**, 417 (1969).
[14] M. C. Curtis, A. P. Levick, and P. J. Sarre, Laser Chem. **9**, 359 (1988).
[15] E. P. Clifford, P. G. Wenthold, W. C. Lineberger, G. A. Petersson, K. M. Broadus, S. R. Kass, S. Kato, C. H. DePuy, V. M. Bierbaum, and G. B. Ellison, J. Phys. Chem. A **102**, 7100 (1998).
[16] L. V. Gurvich, I. V. Veyts, C. B. Alcock, and V. S. Iorish, *Thermodynamic Properties of Individual Substances*, 4th ed. (Hemisphere, New York, 1991).
[17] A. D. Walsh, J. Chem. Soc. 2266 (1953).
[18] H. U. Suter, M. B. Huang, and B. Engels, J. Chem. Phys. **101**, 7686 (1994).

[19] J. L. Wilkerson and W. A. Guillory, J. Mol. Spectrosc. **66**, 188 (1977).
[20] J. M. L. Martin, P. R. Taylor, J. P. Francois, and R. Gijbels, Chem. Phys. Lett. **226**, 475 (1994).
[21] R. T. Bise, H. Choi, and D. M. Neumark, J. Chem. Phys. **111**, 4923 (1999).
[22] R. E. Continetti, D. R. Cyr, D. L. Osborn, D. J. Leahy, and D. M. Neumark, J. Chem. Phys. **99**, 2616 (1993).
[23] D. J. Leahy, D. L. Osborn, D. R. Cyr, and D. M. Neumark, J. Chem. Phys. **103**, 2495 (1995).
[24] D. L. Osborn, H. Choi, D. H. Mordaunt, R. T. Bise, D. M. Neumark, and C. M. Rohlfing, J. Chem. Phys. **106**, 3049 (1997).
[25] D. L. Osborn, D. J. Leahy, D. R. Cyr, and D. M. Neumark, J. Chem. Phys. **104**, 5026 (1996).
[26] F. Arndt., *Organic Synthesis Collective* (Wiley, New York, 1943), Vol. II pp. 165.
[27] J. M. B. Bakker, J. Phys. E **6**, 785 (1973).
[28] J. M. B. Bakker, J. Phys. E **7**, 364 (1974).
[29] D. P. de Bruijn and J. Los, Rev. Sci. Instrum. **53**, 1020 (1982).
[30] M. W. Chase, Jr., J. Phys. Chem. Ref. Data Monogr. **9**, 1 (1998).
[31] Y. Huang, S. A. Barts, and J. B. Halpern, J. Phys. Chem. **96**, 425 (1992).
[32] Z. L. Cai, G. H. Sha, C. H. Zhang, and M. B. Huang, J. Mol. Struct.: THEOCHEM **85**, 303 (1992).
[33] M. C. Curtis, Ph.D. thesis, University of Nottingham.
[34] C. Devillers and D. A. Ramsay, Can. J. Phys. **49**, 2839 (1971).
[35] M. Fujitake, R. Kiryu, and N. Ohashi, J. Mol. Spectrosc. **154**, 169 (1992).
[36] G. Herzberg and D. N. Travis, Can. J. Phys. **42**, 1658 (1964).
[37] V. E. Bondybey and J. H. English, J. Mol. Spectrosc. **70**, 236 (1978).
[38] A. H. Laufer and H. Okabe, J. Am. Chem. Soc. **93**, 4137 (1971).
[39] A. Langer, J. A. Hipple, and D. P. Stevenson, J. Chem. Phys. **22**, 1836 (1954).
[40] G. S. Paulett and P. E. Ettinger, J. Chem. Phys. **39**, 825 (1963).
[41] J. C. Hassler and D. W. Setser, J. Am. Chem. Soc. **87**, 3793 (1965).
[42] W. Braun, A. M. Bass, and M. Pilling, J. Chem. Phys. **52**, 5131 (1970).
[43] G. Leroy and M. Sana, Theor. Chim. Acta **32**, 329 (1974).
[44] J. Lievin and G. Verhaegen, Theor. Chim. Acta **42**, 47 (1976).
[45] M. S. Gordon and S. R. Kass, J. Phys. Chem. **99**, 6548 (1995).
[46] S. P. Walch, J. Chem. Phys. **103**, 4930 (1995).
[47] A. Papakondylis and A. Mavridis, J. Phys. Chem. A **103**, 1255 (1999).
[48] R. N. Zare, Mol. Photochem. **4**, 1 (1972).
[49] S. J. Singer, K. F. Freed, and Y. B. Band, J. Chem. Phys. **81**, 3064 (1984).
[50] A. Friedman, A. M. Soliva, S. A. Nizkorodov, E. J. Bieske, and J. P. Maier, J. Phys. Chem. **98**, 8896 (1994).
[51] F. R. Bennett, J. P. Maier, G. Chambaud, and P. Rosmus, Chem. Phys. **209**, 275 (1996).